

Supporting Information

Two-dimensional B-C-O alloys: a promising 2D material for electronic devices

Si Zhou, Jijun Zhao*

*Key Laboratory of Materials Modification by Laser, Ion and Electron Beams, Dalian University
of Technology, Ministry of Education, Dalian 116024, China*

* Corresponding author: Email: zhaojj@dlut.edu.cn

S1. Dynamical stability

Figure S1 shows the phonon dispersions of various 2D B-C-O hybrid structures. Graphene sheets uniformly doped by B-O, B₂-O and B₃-O units are dynamically stable with a doping rate 1-C% up to 25%, 37.5% and 50%, respectively [Figure S1(a-c)]. For the B-C-O monolayers with B:O = 1:1, the B-O units favor organization into the chain-like structure. The system retains dynamical stability for 1-C% \leq 25% [Figure S1(e)]. Beyond this critical doping rate, the hybrid sheet shows negative frequencies down to -200 cm^{-1} [Figure S1(d)]. This imaginary phonon band is correlated with the out-of-plane vibration of the B-O chains, which are excess in electrons and not compatible with the formation of sp^2 hybridization. The B₃OC₂, BOC₂ and B₆O₃C₅ phases all show stable phonon bands [Figure S1(f-h)].

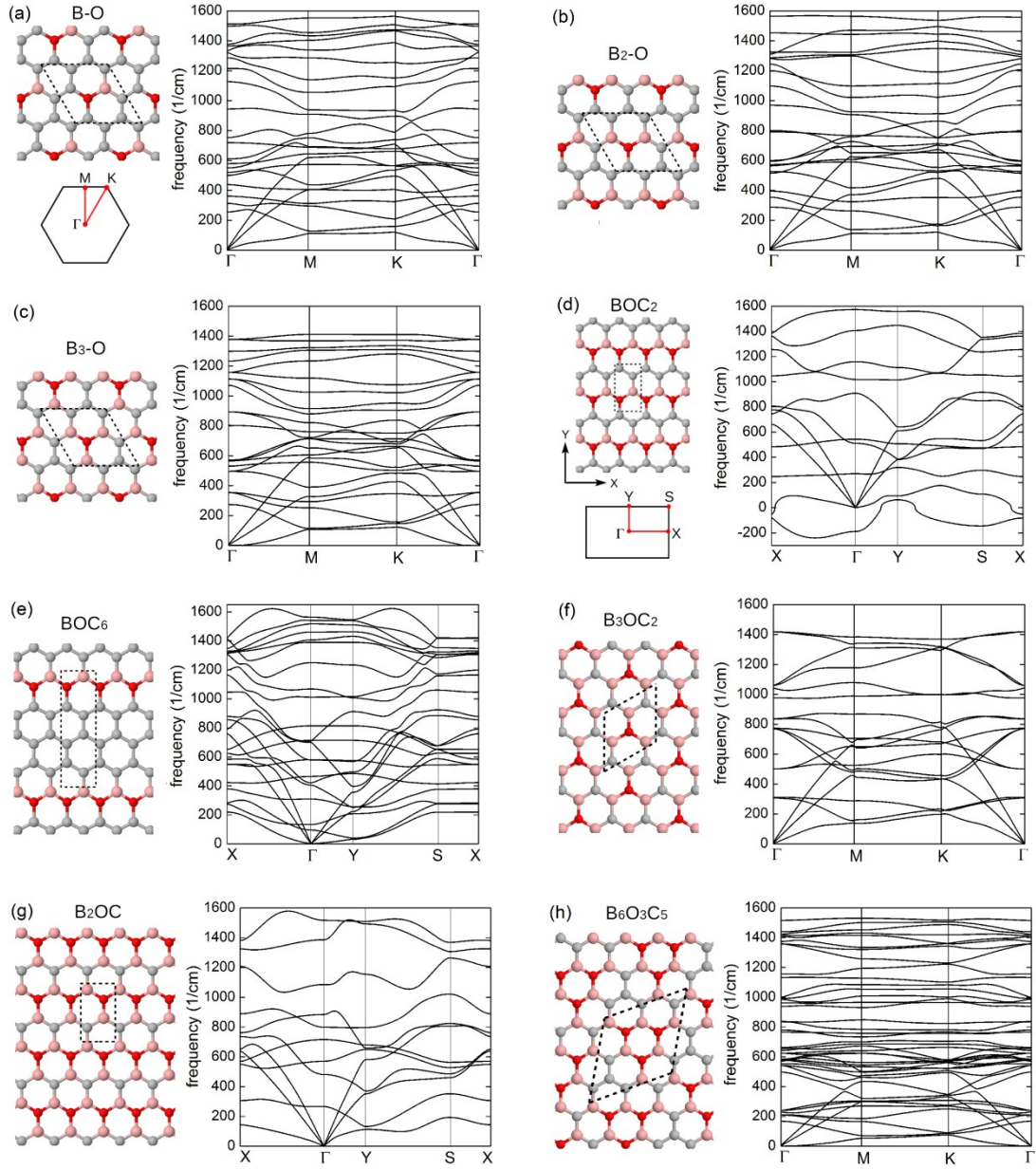


Figure S1. Phonon dispersions of (a) B-O, (b) B₂-O, and (c) B₃-O doped graphene, and (d) BOC₂, (e) BOC₆, (f) B₃OC₂, (g) B₂OC, and (h) B₆O₃C₅ phases. The corresponding atomic structures are shown on the left of phonon bands. The C, O and B atoms are represented in grey, red and peach, respectively. The dashed boxes indicate the unit cells used for the phonon calculations. The Brillouin zone and the representation of high symmetry points are shown in (a) and (d), for the systems with hexagonal (a, b, c, f, h) and rectangular (d, e, g) supercells, respectively.

S2. Electronic band structures

In this work, the electronic band structures of the B-C-O monolayers are calculated by using the HSE06 hybrid functional. To test the performance of different functionals, we compute the band structure of *h*-BN using the PBE, PBE0, and HSE06 functionals, and obtain band gap of 4.63 eV, 6.23 eV, and 5.40 eV, respectively, as shown in Figure S2. The HSE06 functional best reproduces the experimental value of 5.5 eV for *h*-BN,¹ while the PBE and PBE0 functionals underestimate and overestimates, respectively. The dispersions of the electron bands do not explicitly rely on the functional we choose for the calculation, as they give similar values of the effective masses demonstrated in Table S1. Similar results are found for the electronic band structures of B₂OC and B₆O₃C₅ [shown in Figure 2(b, d) of the manuscript]. Therefore, we expect that the present HSE06 hybrid functional method provides reliable results on the electronic properties of the 2D B-C-O systems.

Figure S3 shows the electronic band structures of various 2D B-C-O alloys. The systems with B:O = 1:1 and 3:1 exhibit metallic behaviors due to the excess and deficiency of electrons with respect to graphene, corresponding to the n-type and p-type doping, respectively [Figure S3(a-b)]. The B-C-O sheets with B:O = 2:1 are semiconductors, and the band gap depends on the doping rate 1-C%. In particular, for the B₂-O chain patterned structures [Figure S3(c-f)], the systems have direct band gap of 1.33 eV, 1.59 eV, 2.00 eV, and 2.69 eV for 1-C% = 25%, 37.5%, 50%, and 62.5%, respectively. The band gap decreases as the concentration of B and O species increases. For the B₂-O ring patterned structures [Figure S3(g-h)], the systems show band gap of 1.80 eV and 2.11 eV for 1-C% = 36% and 54%, respectively.

Table S1. The calculated effective masses of *h*-BN of electron (m_e) and hole (m_h) carriers by using the PBE, PBE0 and HSE06 functionals.

Functional	m_e/m_0	m_e/m_0	m_h/m_0	m_h/m_0
	(K \rightarrow Γ)	(K \rightarrow M)	(K \rightarrow Γ)	(K \rightarrow M)
PBE	0.67	1.20	0.58	0.94
PBE0	0.61	1.04	0.53	0.84
HSE06	0.65	1.12	0.55	0.88

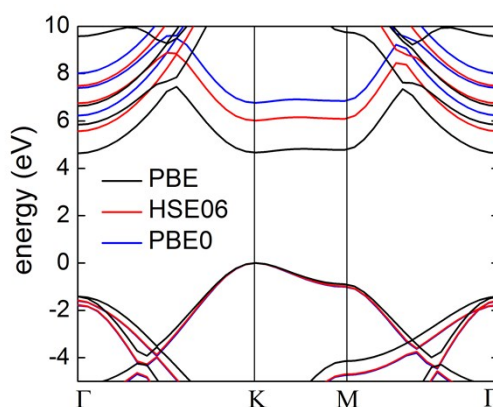


Figure S2. The electronic band structures of *h*-BN calculated by using the PBE, PBE0 and HES06 functionals. The zero energy level is shifted to the top of valence band for comparing the results given by different functionals.

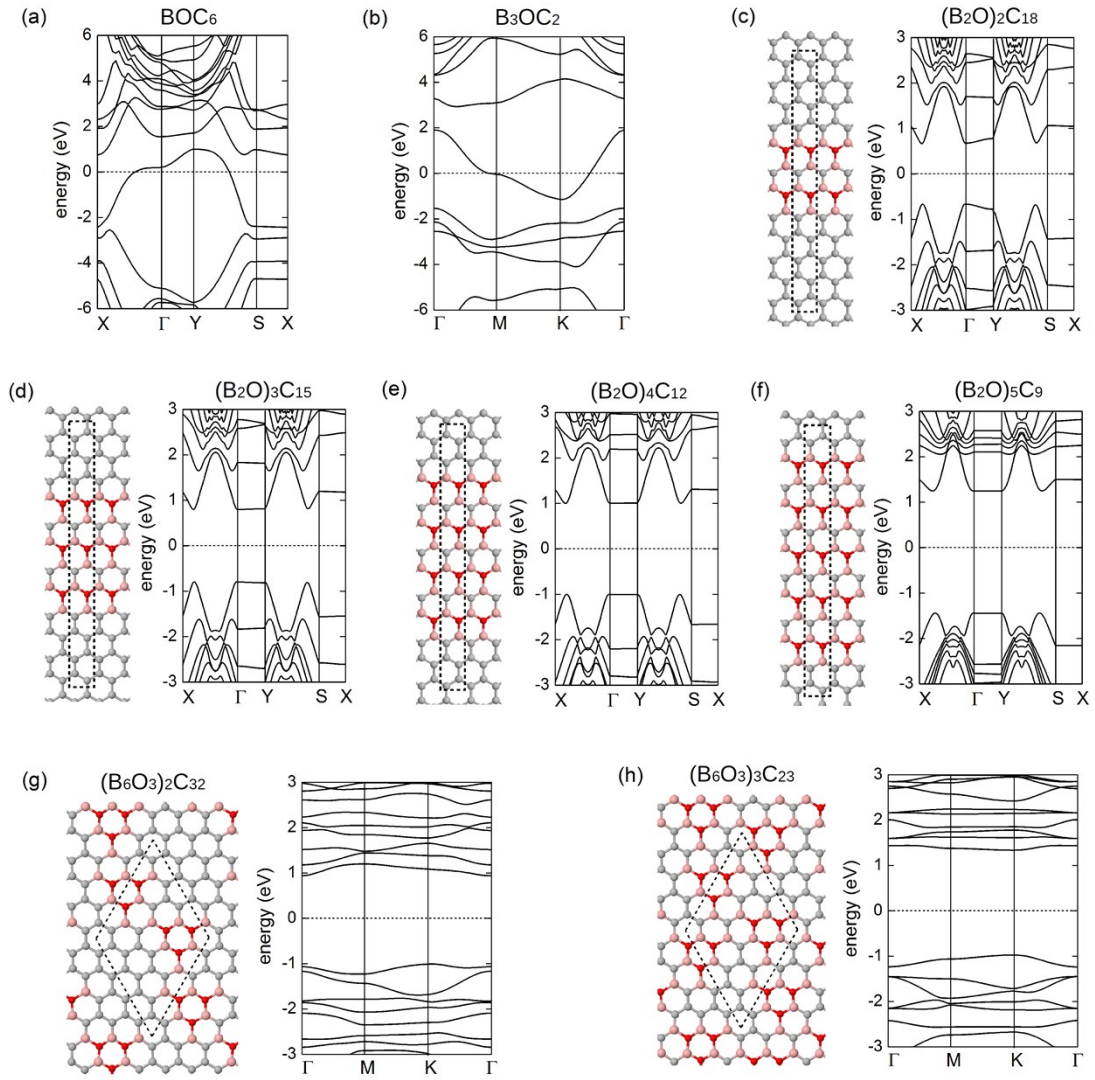


Figure S3. Electronic band structures of (a) BOC_6 , (b) B_3OC_2 , (c) $(\text{B}_2\text{O})_2\text{C}_{18}$, (d) $(\text{B}_2\text{O})_3\text{C}_{15}$, (e) $(\text{B}_2\text{O})_4\text{C}_{12}$, (f) $(\text{B}_2\text{O})_5\text{C}_9$, (g) $(\text{B}_6\text{O}_3)_2\text{C}_{32}$, and (h) $(\text{B}_6\text{O}_3)_3\text{C}_{23}$. The zero energy level is referred to the Fermi energy. The corresponding atomic structures are shown on the left of electron bands. The C, O and B atoms are represented in grey, red and peach, respectively. The dashed boxes indicate the unit cells used for the electronic band structure calculations. The atomic structures for the electronic band in (a) and (b) are shown in Figure S1(e) and (f), respectively. The Brillouin zone and the representation of high symmetry points for the hexagonal and rectangular supercells are shown in Figure S1(a) and (d), respectively.

S3. *Ab initio* molecular dynamic simulation

In order to assess the thermal stability of the 2D B-C-O alloys, we perform *ab initio* molecular dynamics (AIMD) simulation for the B_2OC and $B_6O_3C_5$ systems, within the NVT ensemble at temperature of 1500 K and time step of 1.0 fs. After 20 ps, both systems show temperature-induced lattice distortion, with the largest in-plane and out-of-plane displacement of atoms around 0.35 Å and 0.87 Å, respectively. During the entire AIMD simulation, there is no topological defect generated in the monolayer sheets, confirming the high thermal stability of the B-O-C lattice structures.

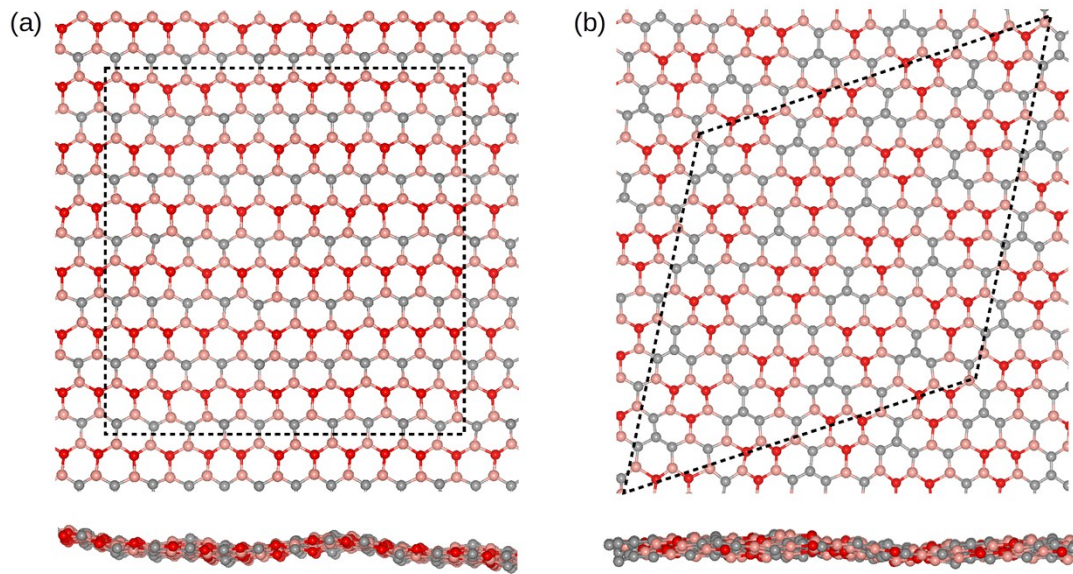


Figure S4. Atomic structures of (a) B_2OC and (b) $B_6O_3C_5$ after 20 ps of AIMD simulations at 1500 K. Upper plots: top-view; lower plots: side-view. The C, O and B atoms are represented in grey, red and peach, respectively. The dashed boxes indicate the supercells used for the calculations.

S4. Other structures in the phase diagram

In the phase diagram Figure 1(c) of the main text, we compare the Gibbs free energy of formation of various 2D B-C-O systems with bulk boron trioxide (B_2O_3) and monolayer graphene oxide (GO). The atomic structures of B_2O_3 solid and GO are shown in Figure S5. We consider the α -phase B_2O_3 (space group $P31$), which is one of the most stable oxidized forms of boron at normal pressure.² It has a trigonal structure characterized by a three dimensional network of corner-linked BO_3 triangles. Depending on the chemical potential of the carbon reservoir, B_2O_3 may emerge in the phase diagram and co-exist with graphene in a phase separation manner. In Figure 1(c), we use the relative fractions of B_2O_3 and graphene with the O:C ratio of 0.1. At higher chemical potential of carbon (C-rich condition), formation of B_2O_3 solid is less favored. For GO, we consider one of the most stable phases – a graphene layer fully covered by epoxide groups (OC_2) as proposed by Šljivančanin *et al.*³, and it only exists in the O-rich and B-poor conditions. At higher chemical potentials of B reservoir, formation of GO cannot compete with that of B_2O_3 , B_2OC , or $B_6O_3C_5$ phases.

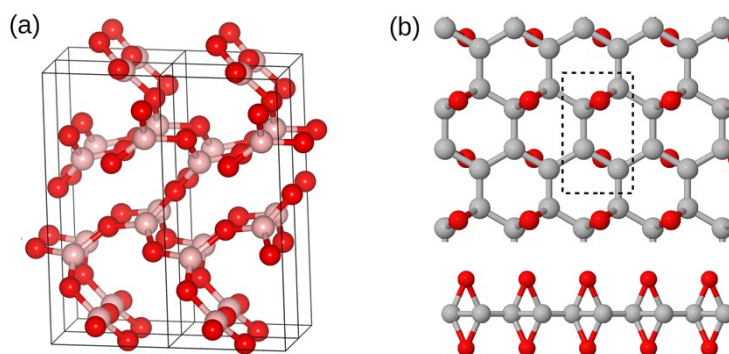


Figure S5. Atomic structures of (a) boron trioxide (B_2O_3) solid, and (b) graphene oxide fully covered by epoxide groups (OC_2). The C, O and B atoms are represented in grey, red and peach, respectively. The black box indicates the unit cells of the two systems.

S5. X-ray photoelectron spectroscopy and Raman spectroscopy signature

The X-ray photoelectron spectroscopy (XPS) core-level energy shifts are calculated for C and O species in various chemical environments in the B-C-O sheets, as shown in Figure S6(a). In particular, we generate norm-conserving pseudopotentials for the ionized C^+ and O^+ species, containing a screened 1s hole in the core.^{4,5} The core-level energy shift at a C (or O) site is given by

$$\Delta C_{1s} = E[C] - E[C^+]$$

where $E[C]$ and $E[C^+]$ are the total energies of the neutral and ionized systems at selected C (or O) site, respectively. The core-level energy shifts evaluated by this method accounts for the vertical photoexcitation transition as well as the core-hole relaxation effects.

For the O 1s XPS, an isolated O atom substituted into graphene (denoted as O-C) exhibits the same core-level shift (ΔO_{1s}) as that of the O species in graphene oxide (the experimental O 1s binding energy is 532 eV⁴), which is used as our reference ($\Delta O_{1s}=0$). The O species in the B_2 -O chains or rings (denoted as O-2B) shows the same ΔO_{1s} as the isolated O atoms in graphene lattice. As the B_2 -O chain or ring-like structures are most energetically favorable in the B-C-O monolayers, the experimentally fabricated samples may exhibit a dominant peak in the O 1s XPS spectra at binding energy of 532 eV. The O species in B-O chains (denoted as O-B) and that bonded with three B atoms (denoted as O-3B) exhibit O 1s energy shifts of 0.7 eV and -1.0 eV, respectively.

For the C 1s XPS, we use the C-C bond as the reference. The C species bonded with B, in which B is adjacent to two O atoms (denoted as C-B2O), has the same core-level energy shifts as that of the C-C bonds. This C-B2O configuration can exist in the form of B_2 -O chains or rings, or B-O rings, as indicated by the green circles in Figure S6(a) (top panels). The C-BO bonds, in which B is bonded with one O atom, exhibit ΔC_{1s} of about -1.4 eV, and are associated with isolated B-O or B_3 -O units embedded in graphene. The C species bonded with isolated O atoms in the sp^2 form shows ΔC_{1s} of about 2.0 eV, the same as that of the O-C bonds in the sp^3 hybridization.⁴

We also calculate the Raman spectra of the B_2OC and $B_6O_3C_5$ phases in comparison with that of graphene and h -BN, based on the linear-response density functional perturbation theory [Figure S6(b)]. Monolayer graphene and h -BN show characteristic peaks at 1570 cm^{-1} and 1340 cm^{-1} , respectively, corresponding to the E_{2g} in-plane vibrational mode, in good agreement with the experimental values of 1580 cm^{-1} and 1350 cm^{-1} .^{1, 6} The B_2OC system shows a dominant peak at 1356 cm^{-1} , and a shoulder peak at 1500 cm^{-1} . The $B_6O_3C_5$ system shows multiple peaks at 1340 - 1430 cm^{-1} , and at 1126 cm^{-1} . The main peaks for in-plane vibrational modes in 2D B_2OC and $B_6O_3C_5$ alloys show red shift with regard to graphene, indicating the weakening of the in-plane covalent bonds within the honeycomb lattice.

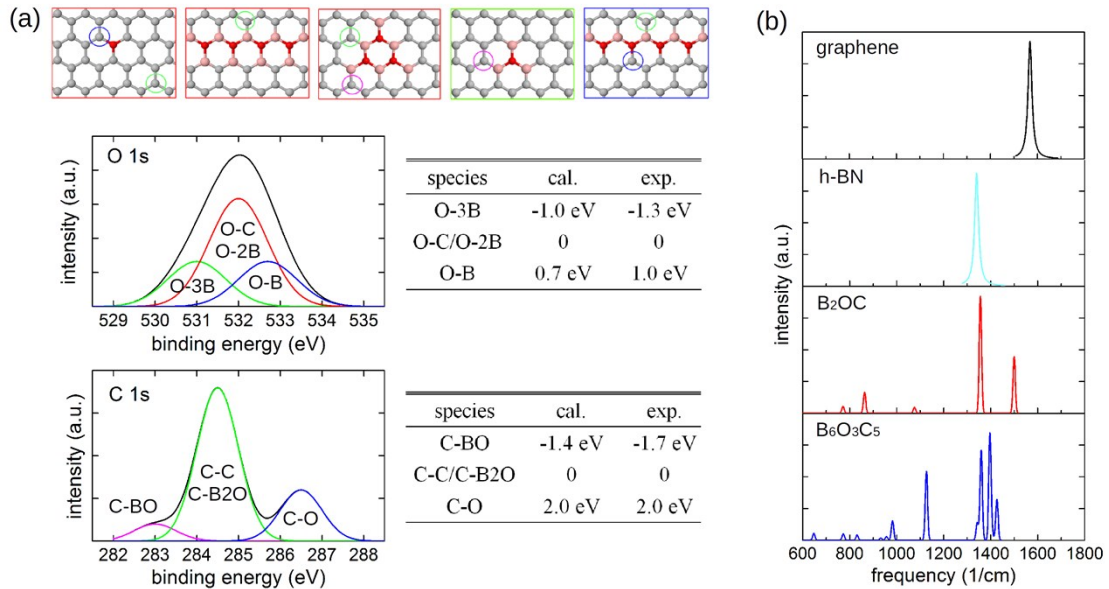


Figure S6. (a) The O 1s and C 1s XPS signature of 2D B-C-O alloy. The top panels in colored boxes show O and C species in various chemical environments in B-C-O sheets. The C, O and B atoms are represented in grey, red and peach, respectively. The two panels on bottom left are schematic O 1s and C 1s XPS spectra. The colored peak of the O (or C) 1s spectra is assigned to the O (or C) species in the rectangular box (or indicated by circles) of the same color. The calculated core-level energy shifts for O and C species are listed in the tables on the right of the XPS spectra, in comparison with the experimental values from Ref⁷. (b) The calculated Raman spectra of B_2OC and $B_6O_3C_5$, in comparison with those of monolayer graphene and h -BN.

S6. Carrier mobility

Here the acoustic phonon-limited carrier mobility μ_{2D} is calculated based on the Takagi model within the deformation potential approximation:⁸⁻¹¹

$$\mu_{2D} = \frac{e\hbar^3 C_{2D}}{k_B T m^* m_d (E_1)^2}$$

where e is the electron charge, \hbar is the reduced Planck constant, k_B is the Boltzmann constant, T is temperature, m^* is the effective mass along the transport direction, m_d is the average effective mass, C_{2D} is the elastic modulus of 2D sheet along the transport direction, and E_1 is the deformation potential constant.

The average effective mass is determined by $m_d = \sqrt{m^* m_{\perp}^*}$, where m_{\perp}^* is the effective mass along the direction perpendicular to the transport direction. The elastic modulus is evaluated by applying a longitudinal strain to the 2D sheet along the transport direction via $C_{2D}(\Delta l/l_0)^2/2 = (E - E_0)/S_0$, where Δl is the strain, l_0 is the equilibrium lattice constant, E_0 and E are the energies of the system before and after applying the strain, and S_0 is the area of the 2D sheet. The deformation potential constant is calculated by the band edge shift under the strain via $E_1 = \Delta V/(\Delta l/l_0)$, where ΔV is the shift of the valence-band minimum (hole carrier) or the conduction-band maximum (electron carrier) upon lattice variation. In practice, we compress and elongate the lattice of B-C-O sheets along the transport direction by 0.5% and 1%, and take the average values for C_{2D} and E_1 .

To test the performance of the above described method, we calculate the electron mobility of *h*-BN, MoS₂ and black phosphorene, as shown in Table S2. Our calculated values are in good agreement with the results from other theoretical work using the same methodology,^{10, 12-14} as well as the experimental values (1~500 cm²V⁻¹s⁻¹ for MoS₂,¹⁵⁻¹⁷ and 40~900 cm²V⁻¹s⁻¹ for black phosphorene¹⁸⁻²⁰). We apply this method for (B₂O)_nC_m and (B₆O₃)_nC_m with chain- and ring-patterned structures, respectively (the results are shown in Table 1 and 2 of the main text).

To investigate the effect of the distributions of the B₂-O chains/rings on the stability and electronic properties of the system, we consider various (B₂O)₂C₁₈ and

$(\text{B}_6\text{O}_3)_2\text{C}_{54}$ models, where the $\text{B}_2\text{-O}$ chains/rings are either closely packed or uniformly distributed within the graphene honeycomb lattice, as shown in Figure S7. All these model structures have the doping rate $1-\text{C}\% = 25\%$. The formation energies are slightly higher when the $\text{B}_2\text{-O}$ chains/rings are uniformly patterned than closely packed (energy difference below 0.1 eV per dopant); accordingly, the formers show smaller band gaps than the latter by up to 0.3 eV. Similar band dispersions are observed for the two $(\text{B}_2\text{O})_2\text{C}_{18}$ structures, as well as for the two $(\text{B}_6\text{O}_3)_2\text{C}_{54}$ models. All these systems present similar values for the effective mass, elastic constant, and deformation potential constant, and consequently their carrier mobilities are comparable to each other, as demonstrated by Table S3.

Moreover, we consider a 2D B-C-O model with mixed $\text{B}_2\text{-O}$ chains and rings ($1-\text{C}\% = 25\%$), as shown in Figure S7(E). This mixed phase is nearly as stable as the pure $(\text{B}_2\text{O})_n\text{C}_m$ and $(\text{B}_6\text{O}_3)_n\text{C}_m$ phases at the same doping rate. It is an indirect gap semiconductor with the top of valence band (VBM) and the bottom of conduction band (CBM) located at the S and Γ point, respectively. The band gap is 1.38 eV, a little smaller than the values of $(\text{B}_2\text{O})_n\text{C}_m$ and $(\text{B}_6\text{O}_3)_n\text{C}_m$ with closely-packed $\text{B}_2\text{-O}$ chains/rings. The carrier mobilities of this mixed phase is moderately reduced due to the increased effective masses with respect to those of $(\text{B}_2\text{O})_n\text{C}_m$ and $(\text{B}_6\text{O}_3)_n\text{C}_m$, as illustrated by Table S3.

Based on the calculations on model A-E, the energetics and electronic properties of the 2D B-C-O alloys are more sensitive to the concentrations of B and O species, and are less affected by the distribution of the $\text{B}_2\text{-O}$ chains/rings within the graphene honeycomb lattice.

Last, we consider graphene sheets uniformly doped by the $\text{B}_2\text{-O}$ units, *i.e.* the $\text{B}_2\text{-O}$ bonds are separated from each other rather than forming chains/rings, such that the system contains O-C bonds, as displayed in Figure S8. These O-C bonds exhibit high ionicity with bond overlap population of about 0.5, which cause charge localization and deteriorate to the charge transport of the system. As demonstrated by Table S4, the systems with $\text{B}_2\text{-O}$ units uniformly substituted into the honeycomb lattice have

larger effective masses and lower carrier mobility than the ring-patterned system at the same doping rate.

Table S2. The calculated electron mobility of *h*-BN, MoS₂, and black phosphorene based on the deformation potential method. The band gap E_g , elastic modulus C_{2D} , effective mass m , the deformation potential constant E_1 , and mobility μ_{2D} for electron carriers are compared with the results from other theoretical work using the same method. For black phosphorene, the x and y axes are taken the same as those of Ref¹¹.

material	E_g	C_{2D} (J/m ²)	m/m_0	E_1 (eV)	μ_{2D} (10 ³ cm ² V ⁻¹ s ⁻¹)
<i>h</i> -BN	5.40	326.30	0.86	5.96	0.25
<i>h</i> -BN (Ref ¹²)	--	285.66	0.97	3.66	0.49
MoS ₂	1.76	123.57	0.53	4.20	0.55
MoS ₂ (Ref ¹⁴)	1.82	139.16	0.48	3.90	0.88
Phosphorene (x)	1.57	40.65	0.15	2.43	2.32
Phosphorene (x) (Ref ¹⁰)	1.51	28.94	0.17	2.72	1.10-1.14
Phosphorene (y)	1.57	110.58	1.27	5.89	0.12
Phosphorene (y) (Ref ¹⁰)	1.51	101.60	1.12	7.11	0.08

Table S3. The calculated band gap E_g and carrier mobility μ_{2D} of various 2D B-C-O systems with the doping rate 1-C% = 25% (the atomic structures are shown in Figure S7). The superscripts x and y denote the zigzag and armchair directions, respectively. The elastic constant C_{2D} , effective mass m , and the deformation potential constant E_1 are also listed.

carrier	system	E_g (eV)	C_{2D}^x (J/m ²)	C_{2D}^y	m_e^x/m_0	m_h^y/m_0	E_1^x (eV)	E_1^y	μ_{2D}^x (10 ³ cm ² V ⁻¹ s ⁻¹)	μ_{2D}^y
e	A	1.33	295.23	280.62	0.13	0.53	2.03	4.42	34.09	2.33
	B	1.15	295.78	282.41	0.15	0.50	2.52	4.13	26.15	2.77
	C	1.64	298.10		0.27		4.42		4.63	
	D	1.36	296.39		0.28		4.21		4.31	
	E	1.28	295.10	279.25	0.10	2.70	2.86	3.00	15.36	0.50
h	A	1.33	295.23	280.62	0.16	1.29	4.80	1.48	3.77	4.81
	B	1.15	295.78	282.41	0.16	1.10	5.00	1.80	3.89	4.17
	C	1.64	298.10		0.27		3.65		6.78	
	D	1.36	296.39		0.36		5.09		2.30	
	E	1.28	295.10	279.25	0.43	2.70	4.01	1.40	0.89	1.09

Table S4. The calculated carrier mobility of $(\text{B}_6\text{O}_3)_1\text{C}_{41}$ (1-C% = 18%) and $(\text{B}_6\text{O}_3)_2\text{C}_{32}$ (1-C% = 36%), where B and O species are either patterned into the ring-like structures [denoted as “ring”, the atomic structures are shown in Figure 3(c) of the main text and Figure S3(g), respectively], or uniformly distributed within the honeycomb lattice in the form of $\text{B}_2\text{-O}$ units (denoted as “uni”, the structures are shown in Figure S8). The band gap E_g , elastic constant C_{2D} , effective mass m , and the deformation potential constant E_1 are also listed.

1-C%	E_g (eV)	C_{2D} (J/m ²)	m_e/m_0	m_h/m_0	E_1^e (eV)	E_1^h (eV)	μ_{2D}^e (10 ³ cm ² V ⁻¹ s ⁻¹)	μ_{2D}^h (10 ³ cm ² V ⁻¹ s ⁻¹)
18% (<i>ring</i>)	1.52	310.31	0.25	0.19	4.39	3.54	6.35	17.91
18% (<i>uni</i>)	1.28	291.00	0.49	0.48	3.84	6.01	1.82	0.77
36% (<i>ring</i>)	1.80	286.83	0.27	0.34	4.49	3.61	4.36	4.16
36% (<i>uni</i>)	1.35	284.53	0.48	0.81	3.88	6.12	1.81	0.25

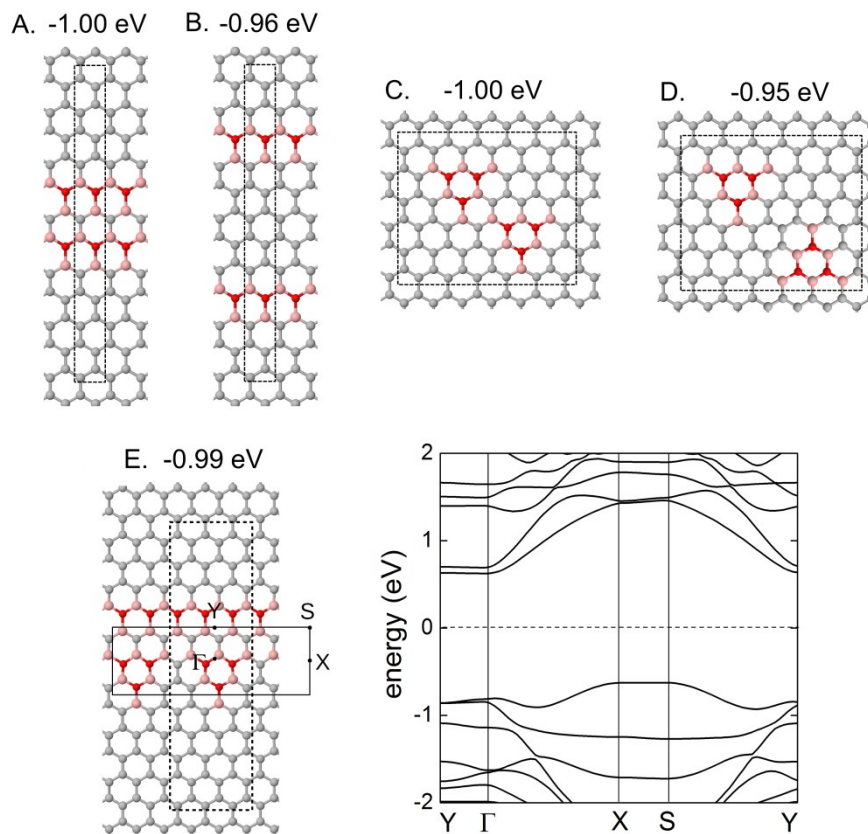


Figure S7. Various 2D B-C-O models with the doping rate $1-C\% = 25\%$. Model A and B (C and D) are $(B_2O)_2C_{18}$ [$(B_6O_3)_2C_{54}$] systems with the two B_2O chains (rings) closely packed and uniformly patterned within the honeycomb lattice, respectively. Model E is a mixed phase of $(B_2O)_nC_m$ and $(B_6O_3)_nC_m$. The C, O and B atoms are represented in grey, red and peach, respectively. The dashed boxes indicate the supercells for each system. The formation energies (per dopant) are shown on top of each system. The electronic band structure of model E is shown on the right of its structure, and the first Brillouin zone is indicated by the solid box in its structure. The Fermi energy is set as zero.

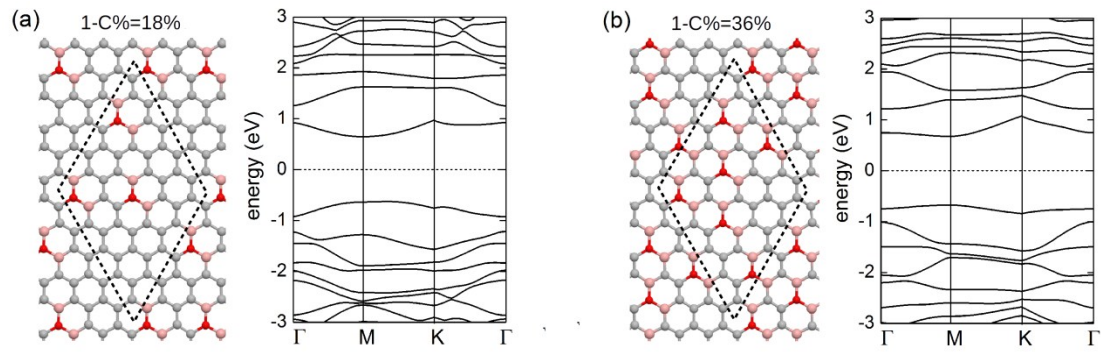


Figure S8. The atomic structures and electronic band structures of graphene monolayer uniformly doped by B₂-O with the doping rate $1-C\% = 18\%$ (a) and 36% (b). The C, O and B atoms are represented in grey, red and peach, respectively. The zero energy level of the electronic band structure is referred to the Fermi energy.

S7. Mechanical properties

We calculate the mechanical properties of B₂OC and B₆O₃C₅ in comparison with monolayer graphene and *h*-BN, by starting from their equilibrium structures and elongating the lattice parameters gradually with a strain step of 0.2%. Uniaxial strain is applied for B₂OC, and biaxial strain is applied for graphene, *h*-BN and B₆O₃C₅. The van der Waals thickness of monolayer B-C-O, graphene or *h*-BN sheets is uniformly taken as 3.35 Å. The Young's Modulus is calculated by $E = \sigma/\varepsilon$ in the linear region of stress-strain (σ - ε) curves, as illustrated in Figure S9. All results on mechanical properties are summarized in Table S5. The obtained Young's modulus, intrinsic strength σ_τ and breaking strain τ of graphene and *h*-BN are in good agreement with the experimental and theoretical values.^{1, 21-24} The B₂OC system exhibit large stiffness and mechanical strength along the zigzag direction – E of 620 GPa and σ_τ of 77 GPa, approaching the values of graphene and *h*-BN, and τ of 28%, even higher than that of graphene. Along the armchair direction, the B₂OC structure is fragile with τ of only 8% due to the weak O-B¹ bonding as illustrated in Figure 3(c) of the main text. The B₆O₃C₅ system shows lower mechanical strength than B₂OC (zigzag direction), with E of 402 GPa, σ_τ of 47 GPa, and τ of 18%.

Table S5. The calculated Young's modulus E , intrinsic strength σ_τ , and breaking strain τ of graphene, h -BN, B_2OC along the zigzag (x) and armchair (y) directions, and $B_6O_3C_5$. Biaxial strains are applied for graphene, h -BN and $B_6O_3C_5$, and uniaxial strain is applied for B_2OC . For graphene and h -BN, our results are compared with the experimental values (exp.) and theoretical values (cal.) of the previous work.

material	E (GPa)	σ_τ (GPa)	τ
graphene (<i>biaxial</i>)	1000	93	20%
graphene (exp. Ref ²¹)	1000	130	25%
graphene (cal. Ref ²²)	1037	100	20%
h -BN (<i>biaxial</i>)	852	81	22%
h -BN (exp. Ref ¹)	872	88	22%
h -BN (cal. Ref ²⁴)	833	83	24%
B_2OC (x)	620	77	28%
B_2OC (y)	579	35	8%
$B_6O_3C_5$ (<i>biaxial</i>)	402	47	18%

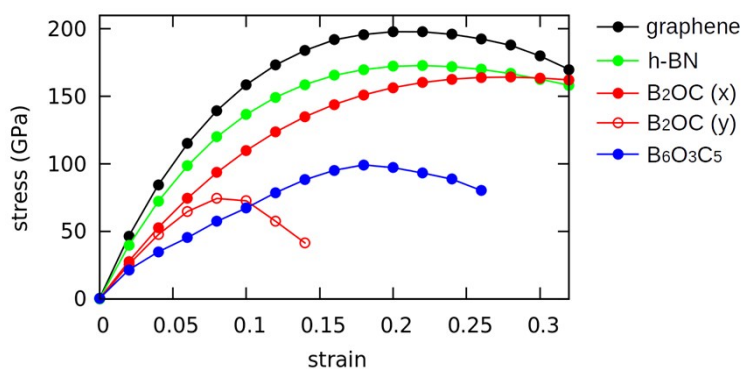


Figure S9. The stress-strain curves for graphene, h -BN, B_2OC along the zigzag (x) and armchair (y) directions, and $B_6O_3C_5$ (biaxial).

S8. Chemical stability

To investigate the chemical stability of the 2D B-C-O alloys, we simulate the oxidation process of a B-C-O sheet by spin-polarized DFT with the nudged elastic band (NEB) method,²⁵ as displayed in Figure S10. As a representative, we consider the $(\text{B}_6\text{O}_3)_3\text{C}_{23}$ model [the structure is shown in Figure S3(h)], with the ring-like structure and B:O = 2:1. The reaction of an O_2 molecule with the B-C-O sheet involves two steps: the adsorption of O_2 on the surface bridging two neighboring B atoms, and then dissociation of O_2 along with the formation of two epoxide groups. The first step requires an activation energy of 0.4 eV, and the transition state occurs when the O_2 molecule has O-O bond length elongated to 1.33 Å and approaches a B atom in the basal plane (O-B distance is 2.20 Å). At this transition state, the O_2 molecule undergoes the triplet-to-singlet spin conversion. This first process leads the system to a metastable state where O_2 bridges two adjacent B atoms in the B-C-O sheet (O-O bond length of 1.49 Å and O-B distance of 1.50 Å), with adsorption energy of 0.77 eV per O atom. (The adsorption energy is defined as $E_{\text{B-C-O}} + 0.5 \times E_{\text{O}_2} - E_{\text{B-C-O}+\text{O}_2}$, where $E_{\text{B-C-O}}$, E_{O_2} , $E_{\text{B-C-O}+\text{O}_2}$ are the energies of the B-C-O sheet, an O_2 molecule, and an O_2 bridge adsorbed on the B-C-O sheet, respectively.) For the second step, the transition state occurs when the O-O bond of the O_2 bridge breaks (O-O distance is 2.04 Å), leading to the formation of two epoxide groups, and the activation energy is 0.5 eV. The adsorption energy of an epoxide group on the B-C-O surface is 1.29 eV.

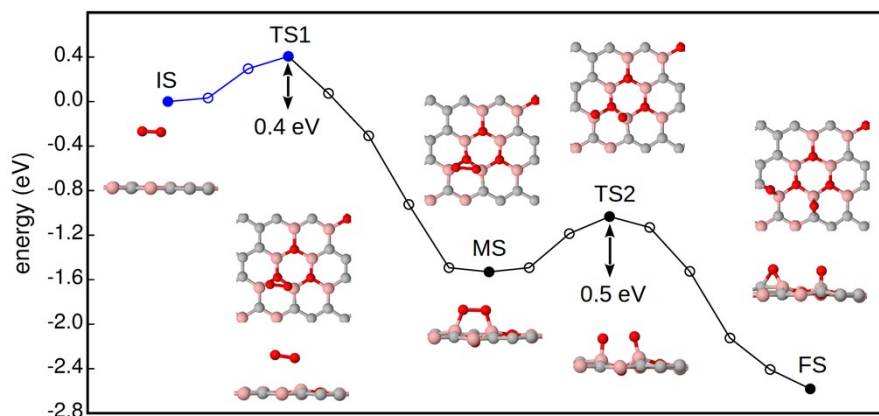


Figure S10. The oxidation process of the 2D B-C-O alloy simulated by spin-polarized DFT with the nudged elastic band method. The $(\text{B}_6\text{O}_3)_3\text{C}_{23}$ model is used for the calculation, and its structure is shown in Figure S3(h). The blue (black) symbols/line indicate the energy points where the O_2 molecule (dissociated O atoms) is in the triplet (single) state. The filled discs (from left to right) represent the initial state (IS), first transition state (TS1), metastable state (MS), second transition state (TS2), and final state (FS), respectively. The energy is referred to that of the initial state. The numbers below TS1 and TS2 indicate the activation energies of the two subsequent processes. The atomic structures (top view and side view) of the system at IS, TS1, MS, TS2 and FS are shown next to their corresponding energy point, respectively. The C, O and B atoms are represented in grey, red and peach, respectively.

References

1. L. Song, L. Ci, H. Lu, P. B. Sorokin, C. Jin, J. Ni, A. G. Kvashnin, D. G. Kvashnin, J. Lou, B. I. Yakobson and P. M. Ajayan, *Nano Lett.*, 2010, **10**, 3209-3215.
2. U. Engberg, *Phys. Rev. B*, 1997, **55**, 2824-2830.
3. Ž. Šljivančanin, A. S. Milošević, Z. S. Popović and F. R. Vukajlović, *Carbon*, 2013, **54**, 482-488.
4. S. Kim, S. Zhou, Y. Hu, M. Acik, Y. J. Chabal, C. Berger, W. de Heer, A. Bongiorno and E. Riedo, *Nat. Mater.*, 2012, **11**, 544-549.
5. S. Zhou, S. Kim and A. Bongiorno, *J. Phys. Chem. C*, 2013, **117**, 6267-6274.
6. A. C. Ferrari and D. M. Basko, *Nat. Nanotechnol.*, 2013, **8**, 235-246.
7. B. Ozturk, A. de-Luna-Bugallo, E. Panaitescu, A. N. Chiaramonti, F. Liu, A. Vargas, X. Jiang, N. Khariche, O. Yavuzcetin, M. Alnaji, M. J. Ford, J. Lok, Y. Zhao, N. King, N. K. Dhar, M. Dubey, S. K. Nayak, S. Sridhar and S. Kar, *Sci. Adv.*, 2015, **1**, e1500094.
8. J. Bardeen and W. Shockley, *Phys. Rev.*, 1950, **80**, 72-80.
9. C. Herring and E. Vogt, *Phys. Rev.*, 1956, **101**, 944-961.
10. J. Qiao, X. Kong, Z.-X. Hu, F. Yang and W. Ji, *Nat. Commun.*, 2014, **5**, 4475.
11. S. Takagi, A. Toriumi, M. Iwase and H. Tango, *IEEE Transactions on*, 1994, **41**, 2363-2368.
12. S. Bruzzone and G. Fiori, *App. Phys. Lett.*, 2011, **99**, 222108.
13. W. Zhang, Z. Huang, W. Zhang and Y. Li, *Nano Res.*, 2014, **7**, 1731-1737.
14. K. Kaasbjerg, K. S. Thygesen and A.-P. Jauho, *Phys. Rev. B*, 2013, **87**, 235312.
15. RadisavljevicB, RadenovicA, BrivioJ, GiacomettiV and KisA, *Nat. Nanotechnol*, 2011, **6**, 147-150.
16. M. S. Fuhrer and J. Hone, *Nat. Nanotechnol.*, 2013, **8**, 146-147.
17. K. Kaasbjerg, K. S. Thygesen and K. W. Jacobsen, *Phys. Rev. B*, 2012, **85**, 115317.
18. V. Tayari, N. Hemsworth, I. Fasih, A. Favron, E. Gaufres, G. Gervais, R. Martel and T. Szkopek, *Nat. Commun.*, 2015, **6**, 7702.
19. J. D. Wood, S. A. Wells, D. Jariwala, K.-S. Chen, E. Cho, V. K. Sangwan, X. Liu, L. J. Lauhon, T. J. Marks and M. C. Hersam, *Nano Lett.*, 2014, **14**, 6964-6970.
20. H. Liu, A. T. Neal, Z. Zhu, Z. Luo, X. Xu, D. Tománek and P. D. Ye, *ACS Nano*, 2014, **8**, 4033-4041.
21. C. Lee, X. Wei, J. W. Kysar and J. Hone, *Science*, 2008, **321**, 385-388.
22. L. Liu, J. Zhang, J. Zhao and F. Liu, *Nanoscale*, 2012, **4**, 5910-5915.
23. S. M. Kim, A. Hsu, M. H. Park, S. H. Chae, S. J. Yun, J. S. Lee, D.-H. Cho, W. Fang, C. Lee, T. Palacios, M. Dresselhaus, K. K. Kim, Y. H. Lee and J. Kong, *Nat. Commun.*, 2015, **6**, 8662.
24. Q. Peng, W. Ji and S. De, *Comput. Mater. Sci.*, 2012, **56**, 11-17.
25. G. Henkelman, B. P. Uberuaga and H. Jónsson, *J. Chem. Phys.*, 2000, **113**, 9901-9904.